RESEARCH ARTICLE | OCTOBER 04 2024

Multi-mode interference waveguide chip-scale spectrometer (invited)

Md Nafiz Amin ; Vahid Ganjalizadeh ; Tyler J. Adams; Porter B. Dixon ; Zoe Weber ; Matthew DeMartino ; Kevin Bundy ; Aaron R. Hawkins ; Holger Schmidt

APL Photonics 9, 100802 (2024)
https://doi.org/10.1063/5.0222100

Multi-mode interference waveguide chip-scale spectrometer (invited)

Cite as: APL Photon. 9, 100802 (2024); doi: 10.1063/5.0222100
Submitted: 5 June 2024 • Accepted: 15 September 2024 •
Published Online: 4 October 2024

Md Nafiz Amin,[1,a)] Vahid Ganjalizadeh,[1] Tyler J. Adams,[2] Porter B. Dixon,[2] Zoe Weber,[1] Matthew DeMartino,[3] Kevin Bundy,[3] Aaron R. Hawkins,[2] and Holger Schmidt[1]

AFFILIATIONS

[1] ECE Department, UC Santa Cruz, 1156 High Street, Santa Cruz, California 95064, USA
[2] ECEn Department, Brigham Young University, 450 Engineering Building, Provo, Utah 84602, USA
[3] Astrophysics and Astronomy Department, UC Santa Cruz, 1156 High Street, Santa Cruz, California 95064, USA

[a)] **Author to whom correspondence should be addressed:** mdamin@ucsc.edu

ABSTRACT

Spectral analysis of light is one of the oldest and most versatile scientific methods and the basis of countless techniques and instruments. Miniaturized spectrometers have recently seen great advances, but challenges remain before they are widely deployed. We report an integrated photonic spectrometer that achieves high performance with minimal component complexity by combining imaging of light propagation patterns in multi-mode interference waveguides with machine learning analysis. We demonstrate broadband operation in the visible and near-infrared, 0.05 nm spectral resolution, and an array of four spectrometers on a single chip. Two canonical applications are implemented: spectral analysis of the solar spectrum with neural network reconstruction and detection of Rayleigh scattering from microbeads on an optofluidic chip using principal component classification. These results illustrate the potential of this approach for high-performance spectroscopy across disciplines.

I. INTRODUCTION

Spectroscopic analysis of electromagnetic radiation dates back to the days of Newton and has been an invaluable cornerstone of scientific inquiry and a plethora of applications ever since. One major area of inquiry is astronomy where spectral analysis reveals the composition and movement of extraterrestrial objects, such as the Doppler shift analysis of exoplanets.[1,2] Biochemical analysis and medical diagnostics comprise another broad area that extensively utilizes spectral techniques involving continuous spectra (e.g., Raman spectroscopy[3]) or distinct and discretely colored labels that enable multiplexed analysis. Example applications of the latter type include fluorescence imaging of cells[4] and molecular biomarker detection techniques, e.g., barcode assays,[5] nucleic acid labeling,[6] and antibody labeling.[7] More broadly, spectroscopy touches every human industry and intellectual pursuit, from telecommunications to food inspection to art restoration.

The most fundamental performance characteristic of a spectrometer is its spectral resolution $\Delta\lambda$ or resolving power $\lambda/\Delta\lambda$, i.e., the ability to distinguish signals at different wavelengths. For centuries, these quantities have been optimized by maximizing the spatial separation between wavelengths with dispersive elements such as prisms and diffraction gratings. Long beam paths result in larger separations, and, thus, high-performance spectrometers tended to be benchtop-size or larger. However, there are powerful reasons for miniaturizing spectrometers, including size, cost, portability, and elimination of moving parts. In addition, chip-scale integration enables the creation of spectrometer arrays and combining spectral analysis with other functionalities, for example, in a lab-on-chip context.

Arguably, the miniaturization of optical spectrometers is entering a golden age.[8] While early attempts focused on scaling down the traditional dispersion-based approach,[9,10] with correspondingly compromised performance, a number of novel and creative ideas have surfaced in the past two decades, fueled by developments in fabrication technology and computational methods and pushing toward advanced system integration such as smartphone-based spectrometers.[11–13] These ideas have resulted in completely new

categories of spectrometers with a broad range of physical implementations. These include narrowband filters,[14,15] Fourier transform spectrometers,[16,17] and optoelectronic devices with a spectrum-specific response.[18] Reconstructive spectrometers have received the biggest attention and have shown tremendous promise.[8] Here, spectral analysis is based on computational analysis of an image to extract the desired information. These image-generating features are often already designed with micro- and nanofabrication in mind. Moreover, the reliance on computational techniques to determine a spectrum takes advantage of signal processing and continuously improving machine learning algorithms, which can be capable of handling the complications due to low signal-to-noise ratios and fabrication imperfections that are inherent to miniaturization. Examples of this emerging approach include the generation of speckle patterns from disordered waveguide structures,[19] transmission through a plasmonic nanohole array,[20] scattering from multi-mode spiral waveguides,[21] cascaded Mach–Zehnder interferometers,[22] long fibers,[23] or tapered multi-mode fibers.[24,25]

Here, we introduce a new kind of reconstructive integrated spectrometer for high-performance applications. It is based on imaging the wavelength-dependent light propagation patterns in multi-mode interference (MMI) waveguides[26,27] and analyzing the spectral content of these images with suitable machine learning (ML) techniques. The approach can be implemented in any integrated photonic format with wide latitude in device materials, dimensions, fabrication processes, and targeted spectral range. Moreover, it is well suited for integration into a larger analytical system. The reliance on post-imaging, ML-based analysis allows for strongly relaxed design tolerances, thus ensuring low complexity and cost. We demonstrate highly accurate spectral reconstruction of both narrow and broadband spectra in both the visible and near-IR range with a spectral resolution of $\Delta\lambda = 0.05$ nm and resolving power 16 000. We also report a 4×4 array in which four MMI waveguide spectrometers analyze light from four independent fiber-coupled sources simultaneously and with uncompromised performance, demonstrating the scalability of this approach. We illustrate the current performance and future potential of the MMI spectrometer with two canonical applications: The first is the use of the device as an astrophotonic instrument. Sunlight captured by a telescope is introduced into a silicon-based spectrometer chip at the nanowatt power level, and the continuous, broadband spectrum is identified using a convolutional neural network. Second, we demonstrate the incorporation of the spectrometer into a lab-on-chip device for optofluidic particle analysis. Here, an MMI waveguide section is integrated with a microfluidic channel on a PDMS (polydimethylsiloxane) chip, and the Raleigh scattering from single microbeads flowing through the channel is spectrally classified by MMI imaging and principal component analysis. These representative implementations highlight the versatility of the approach and point to its highly customizable use in numerous application settings.

The integrated MMI spectrometer consists of two components: a photonic chip to visualize a spectrum and a machine learning process for spectral reconstruction. The concept and its incorporation into a complete workflow are shown in Fig. 1(a).

The light spectrum to be analyzed is fed into a single-mode waveguide on a chip. The light from remote sources can be coupled into the chip via free-space optics or optical fiber, and we will focus on this arrangement for most of this paper. An alternative approach is to couple light that is generated on the chip itself into the single-mode input waveguide of the spectrometer. This implementation is discussed in the second application to illustrate the seamless integration of the spectrometer in a lab-on-chip device. The light then enters a wider, multi-mode interference waveguide section where the light propagation pattern varies strongly with wavelength. The pattern is imaged with a camera that is typically, but not necessarily, placed over the chip, and the recorded waveguide pattern image is then translated into a spectrum by a machine learning algorithm that can be chosen depending on the application. In this work, we discuss

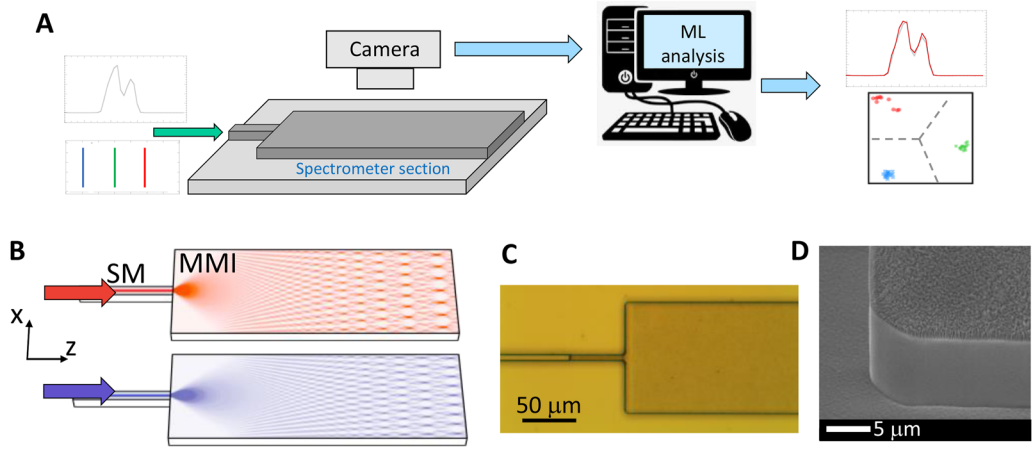

FIG. 1. MMI spectrometer. (a) Schematic overview of the approach. A continuous or discrete spectral signal is coupled into a chip with a multi-mode interference (MMI) waveguide. The wavelength-dependent propagation in the MMI section is imaged by a camera and analyzed by an appropriate machine learning algorithm to reconstruct the spectrum. (b) Visualization of the MMI propagation patterns at two different wavelengths. (c) Microscope image of SU-8 waveguide on silicon. (d) SEM close-up shows roughened surface to enhance out-of-plane light scattering for top-down imaging.

the use of a convolutional neural network (CNN) for the analysis of both narrow and broadband continuous spectra and principal component analysis (PCA) for spectral classification of a finite number of distinct wavelengths.

II. MMI SPECTROMETER PRINCIPLE AND DEVICE IMPLEMENTATION

Figure 1(b) illustrates the physical concept behind the MMI spectrometer. Briefly, a single-mode (SM) input waveguide sustains a single lateral mode with a profile given by $\Psi_0(x)$. At z = 0, the SM waveguide expands into a wider MMI section in which multiple lateral modes $\Psi_m(x)$ exist. The input field is distributed among the multiple mode with amplitude coefficients c_m given by

$$c_m \propto \int \Psi_0(x)\Psi_m(x)dx. \tag{1}$$

The signal then propagates along the multi-mode waveguide according to

$$\Psi(x,z) = \sum_m c_m \Psi_m(x).e^{-i\beta_m z}, \tag{2}$$

where β_m is the propagation constant of the mth mode. Because all the β_m values are different from each other, the phase relation between different modes changes along the waveguide, and characteristic field and intensity patterns ensue. In addition, β_m is wavelength dependent, and as a result, the propagating interference patterns vary deterministically with wavelength as described by Eq. (2). Simulations of these patterns for two representative wavelengths are shown in Fig. 1(b) and illustrate how spectral information is mapped deterministically into the spatial domain.

We developed a standalone, silicon-based spectrometer chip that implements this principle using SU-8 polymer waveguides on silicon dioxide. Figure 1(c) shows a microscope image with a top-down view of the intersection area between the input and MMI waveguide sections. Both waveguides are fabricated in the same lithography step and have a height of 5 μm. The input waveguide is 4 μm wide, while the MMI spectrometer section is 100 μm wide. To facilitate efficient out-of-plane scattering of light out of the MMI waveguide for easy observation from the top, we perform a shallow etch on the MMI section using an oxygen plasma in a reactive-ion-etch chamber that creates a rough top layer with ~300 nm tall nanoscale features ("nanograss"). A magnified view of the MMI surface is shown in the scanning electron microscope (SEM) image in Fig. 1(d). The details of the full fabrication process are provided in the supplementary material.

It is important to note that the spectral analysis is not carried out analytically, i.e., by directly calculating the input spectrum from the observed scattered interference pattern using Eq. (2) as this would require precise knowledge of and control over all fabrication and material parameters. Instead, we use machine learning algorithms that pick up on differences between patterns and that can be trained with signals at known wavelengths. Consequently, our fabrication tolerances are very relaxed, i.e., high accuracy for waveguide height, width, and etch depth is not required, minimizing the complexity of this approach and making it easy to implement in different waveguide systems.

III. MMI SPECTROMETER OPERATION AND PERFORMANCE

The performance of the MMI spectrometer chip was first tested in the infrared wavelength range of around 800 nm. This regime is very attractive for many applications (e.g., astronomy and chemistry) and allowed us to explore the performance limit of the current device. We used a femtosecond Ti:sapphire laser (Trestles 100M, Del Mar Photonics) to create the training images for the neural network. The laser is tunable with 0.05 nm steps and has narrow linewidths when operated in the cw mode. To explore the resolution limit of this configuration, we created training images between 793.8 and 795.6 nm with 0.05 nm step size in several wavelength groups that were determined by the tuning capabilities of the laser. The FWHM of each wavelength is 0.05 nm, ensuring some overlap between the training signals for continuous coverage of the entire bandwidth. The details of this setup and training process are provided in the supplementary material. Each wavelength was fiber-coupled ten times into the MMI chip to create slightly different mode excitation conditions for a total of 250 scatter images. A 952 × 95 μm^2 area of the image near the end of the MMI section was selected to define 1200 × 120 pixels whose amplitudes were used as input to train a 2D convolutional neural network (CNN). In addition to the single-wavelength images, we created broadband spectra from linear combinations with randomly generated amplitudes at each wavelength. This produced an additional 6000 training images; 90% of these images were used for training, while 10% of the images were withheld for testing. After training was completed [see supplementary material for details and Fig. S2(B) for a visualization of the convergence of the process], we first tested the ability of the device to recognize the narrowband spectra. To this end, the CNN was exposed to previously unseen images from the test set, and the predicted amplitudes at each of the possible wavelengths were determined. A representative result for a spectrum with a peak at 794.75 nm is shown in Fig. 2(a).

The gray line represents the spectrum as measured with a conventional, commercial optical spectrum analyzer (OSA). It is virtually indistinguishable from the CNN analysis of the MMI scatter image (red line), showing an excellent agreement of both the peak wavelength and the FWHM. We repeated this experiment at each of the 26 wavelengths in our test interval and found an excellent wavelength in every case as seen in Fig. 2(b), where every CNN-determined wavelength falls within a 0.05 nm band (blue area). Thus, we find a spectral resolution of 0.05 nm and equivalently a resolving power of $R = \lambda/\Delta\lambda = 16\,000$ in this wavelength range. The resolution and bandwidth are limited by the setup, specifically the finite width of the training spectra and the tuning range of the Ti:sapphire laser (see supplementary material for details). We note that, in the telecom wavelength range, this resolving power corresponds to a resolution of 0.1 nm, well below the 0.8 nm (100 GHz) spacing between wavelength division multiplexing channels.

We then assessed the ability to analyze broad, continuous spectra. To this end, a test image was generated using a new, linear combination of the test spectra with randomly generated weights. Figure 2(c) shows that the CNN was able to extract the spectrum from this single, composite scatter image with excellent qualitative agreement in recognizing the spectral features and confirming the 0.05 nm resolution with a continuous spectrum. Finally, we fed light from a different source than was used for generating the training

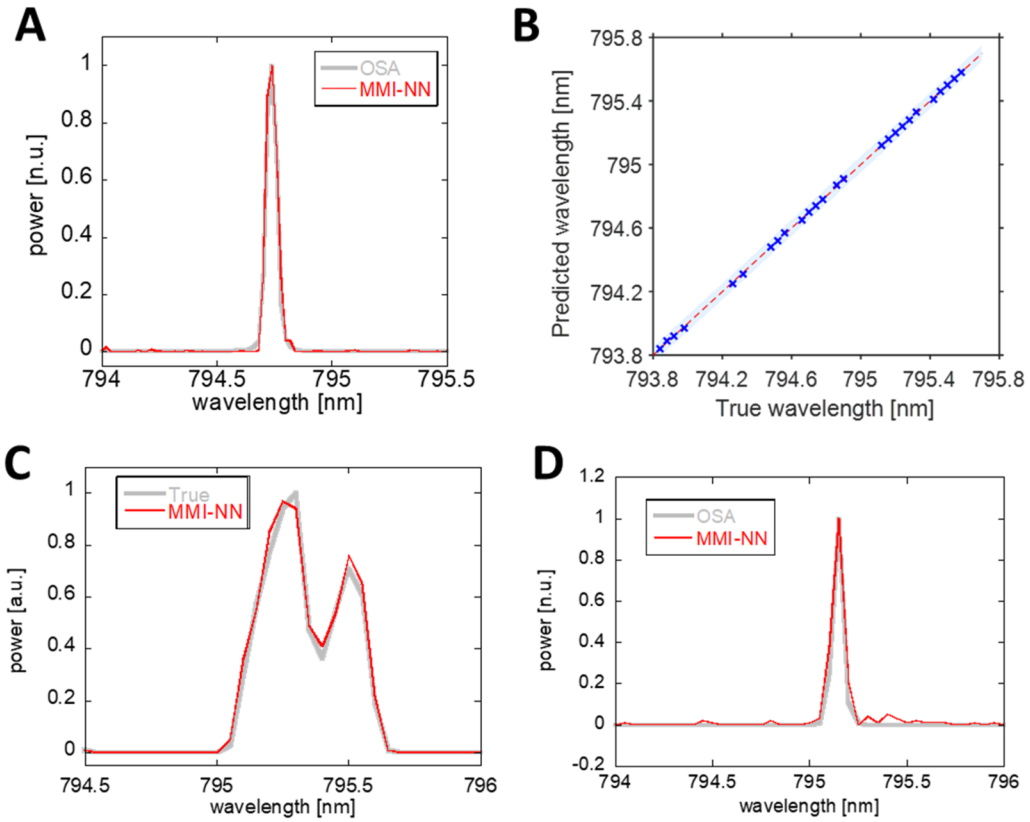

FIG. 2. MMI spectrometer chip performance. (a) Comparison of laser spectrum determined from optical spectrum analyzer (OSA, gray line) and neural network analysis of MMI scatter pattern (red line). (b) Reconstructed vs true peak wavelength of tunable laser spectra, showing a spectral resolution of 0.05 nm as indicated by the blue band. (c) Comparison of NN-reconstructed broadband spectrum (red line) with broad spectrum composed of a linear combination of single-wavelength spectra with different weights (gray line). (d) NN reconstruction (red line) of unseen DBR laser line and OSA reference (gray line).

images into the chip. Specifically, we used light from a distributed Bragg reflector (DBR) diode laser (Vescent Photonics). Again, the spectrum was first recorded with a conventional OSA (gray line in Fig. 2(d). Both the peak wavelength at 795.2 nm and the width of the spectrum are identified correctly by the CNN algorithm.

Figures 2(a)–2(d) represent the core capabilities of a spectrometer. We repeated this assessment in the visible range with a different test source and found comparable performance with a (test source limited) resolution of 0.1 nm over a 10 nm bandwidth. A detailed discussion of the results in the visible spectrum is given in the supplementary material.

A. MMI spectrometer array

Next, we turn our focus toward the advantages that the chip-scale photonic integration offers to open new avenues for applications. The planar and linear nature of the MMI waveguide architecture naturally suggests the addition of multiple waveguides to form highly compact spectrometer arrays. We demonstrate this concept with a 4 × 4 (four inputs, four MMI sections) spectrometer array that is designed to interface with off-the-shelf photonic components. Figure 3(a) shows a commercial 4x single-mode fiber (SMF) coupler array (OzOptics SM fiber V-groove assembly) commonly used with planar lightwave circuit (PLC) splitters and wavelength division multiplexing (WDM) components in fiber-optic networks. Here, it is aligned to the 4 × 4 spectrometer chip and its four independent fibers are simultaneously excited with four laser signals (red arrows).

The commercial fiber coupler terminates in four single-mode fibers that are arranged on an array of V-groove slots with 127.5 μm spacing on a silicon chip. Consequently, we designed and fabricated an MMI spectrometer chip in which four input waveguides have the same spacing, each leading to a separate MMI section as seen in the photograph in Fig. 3(b). All four MMI sections were then simultaneously excited by four independent input signals and a single camera image was taken to record all four spectra in one image [Fig. 3(c)]. We note that the scatter patterns differ between the MMIs due to random variations in surface roughness and slight alignment differences. However, this is not an issue as each MMI spectrometer was trained individually over a region of interest (ROI) marked with red rectangles in Fig. 3(b). When CNN analysis was carried out with unseen images at different wavelengths similar to Fig. 2(b), all four MMI spectrometers showed the same, uncompromised performance as seen in Figs. 3(d)–3(g) because each spectrometer was

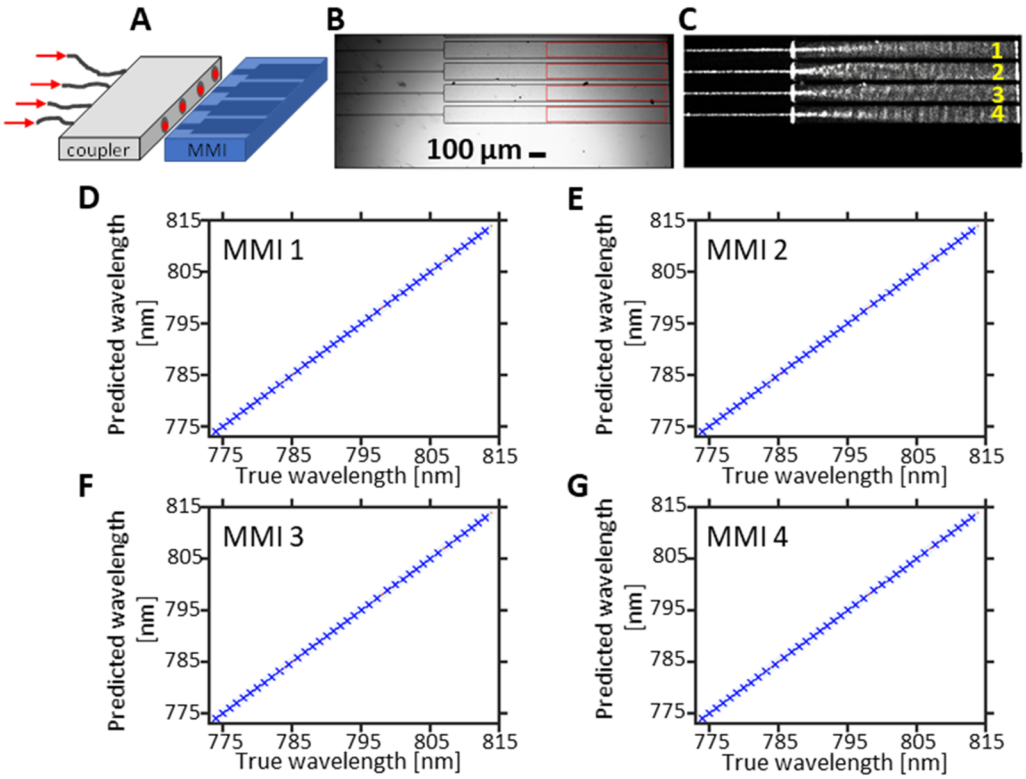

FIG. 3. 4 × 4 MMI spectrometer array. (a) Schematic view of four independent signals fed into MMI spectrometer chip via commercial fiber coupler. (b) Photograph of 4 × 4 MMI spectrometer array. The red rectangles denote the image areas used for individual CNN training and testing. (c) Camera image of scatter image from all four MMI spectrometers. (d)–(g) Accuracy and resolution of the four spectrometers after being individually trained by neural networks.

capable of correctly identifying the peak wavelength of the input signal across a 40 nm bandwidth (1 nm steps). These data also indicate that there is no cross-talk between these narrowly spaced spectrometers during image acquisition. These results show that the expansion of the MMI spectrometer device into highly multiplexed arrays is straightforward as no additional fabrication step is required. Here, we have demonstrated a 4 × 4 array on a chip area of 0.5 × 5 mm^2, and numerous implementations of this concept can be envisioned. These include feeding signals from different sources into an N × N array or building 1 × N arrays in which a single input signal is distributed into N spectrometer sections that could be lithographically integrated with active photonic components on a photonic integrated circuit (PIC) and functionalized for different purposes. For the device dimensions used in this experiment, N can exceed 750 across the diameter of a 4-in. wafer. While the training images for all waveguides were recorded simultaneously [Fig. 3(c)], a CNN was trained separately for each waveguide. To minimize training time and scale to large array sizes, the fabrication can be optimized to produce more uniform waveguides. Alternatively, more advanced neural network training techniques (e.g., transfer learning) can be employed.[28]

B. Application: Broadband astronomical observation

We now illustrate the versatility of the MMI spectrometer and its potential for use in a wide range of research and technology areas. The first of these is astronomy, which has relied on spectral analysis for centuries.[29] The field is now moving toward the collection of vast numbers (10^9) of spectra[30,31] and an increased incorporation of photonics[32] for studies of stars, galaxies, and dark matter.[33–35] For a proof-of-principle demonstration of the suitability of our integrated spectrometer, we set up a solar observation experiment as shown in Fig. 4(a).

The sunlight collected with a small 72 mm telescope (Astro-Tech AT72ED) was captured with a multimode fiber (MMF) placed in the focal plane of the instrument. Approximately 100 m of MMF was used to guide the sunlight to the MMI spectrometer laboratory setup where it is recoupled into a single-mode fiber (SMF) both with and without a 50 nm bandpass (BP) filter centered at 775 nm. The SMF was then coupled into an OSA or the MMI chip for spectral analysis of the solar spectrum. Figure 4(b) shows the OSA recording, showing characteristic Fraunhofer absorption lines in the solar spectrum. The red bar shows the portion of the spectrum that is transmitted through the bandpass filter. The neural network

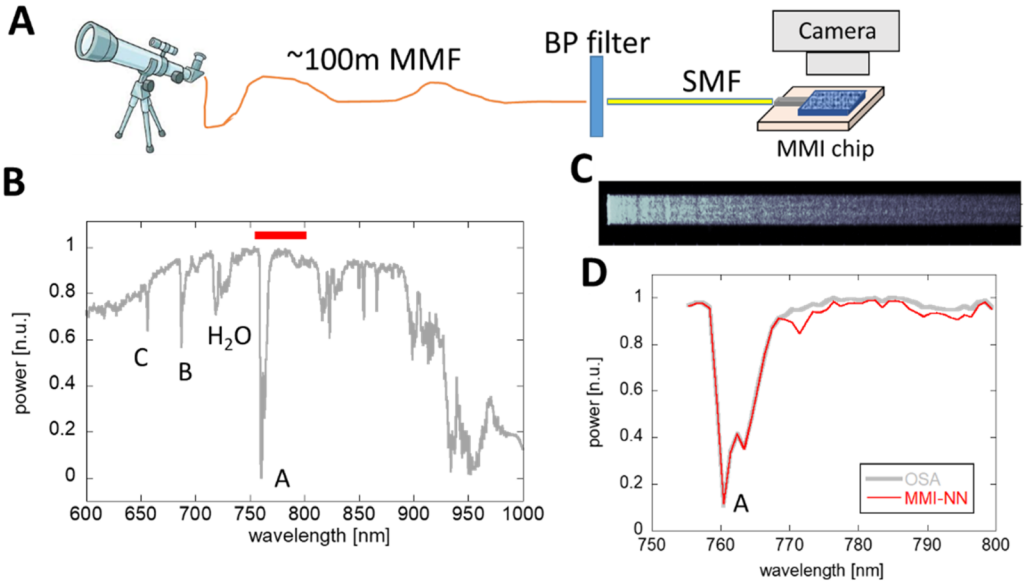

FIG. 4. Solar spectrum analysis with MMI spectrometer. (a) Schematic view of setup to analyze solar spectrum on MMI-spectrometer chip. (b) Full solar spectrum recorded with OSA at SMF output (labels: Fraunhofer lines; red bar: spectral range selected by bandpass filter). (c) MMI scatter pattern of sunlight recorded with 50 nm bandpass filter. (d) CNN-reconstructed solar spectrum (red line) and bandpass-filtered OSA reference spectrum (gray line) around the Fraunhofer A line.

was trained with MMI scatter images [Fig. 4(c)] and a combination of laser peaks at 1 nm spacing from a supercontinuum white light source (NKT) and the continuous sunlight training spectra (see supplementary material for more details). The network was then exposed to an unseen scatter image of the pure sunlight spectrum shown in Fig. 4(d) (gray line), and the resulting spectrum (red line) reproduced the solar spectrum and the Fraunhofer A line (absorption from terrestrial oxygen) very well. Figure 4(d) shows that the MMI spectrometer has the potential for integration with larger telescopes where starlight can be successfully coupled into single-mode fiber for further analysis.[36] This demonstrated that the capability of identifying spectra from remote sources can be applied in numerous other scenarios, including environmental monitoring of pollutant gases[37] or the chemical analysis of aerosols.

C. Application: Classification of single-particle scattering in lab-on-chip device

The second application case is the optofluidic detection of single particles on a chip. The incorporation of miniaturized spectrometers in a lab-on-chip format has been identified as a highly desirable and impactful way to leverage the reduced device size[8] and enable on-chip chemical and biological analysis such as Raman spectroscopy or multiplex detection of fluorescent molecules. Over the past years, optofluidic devices that combine photonic waveguides with microfluidic channels have been developed,[38–40] providing an ideal platform for adding a dedicated spectrometer section. Here, our goals are to demonstrate that the MMI spectrometer can be seamlessly incorporated into an optofluidic device for single-particle analysis, and to show that the spectrometer works with different waveguide materials and that other machine learning techniques can be applied, depending on the purpose.

We use a polydimethylsiloxane (PDMS) platform that has been previously used for fluorescence detection of single biomolecules in combination with microfluidic sample preparation and on-chip laser excitation.[41–43] The device layout used in this study and a photograph of a complete device are shown in Figs. 5(a) and 5(b), respectively, while more details regarding the fabrication and the full experimental setup are described in the supplementary material.

The device consists of a fluidic channel (cross-section $6 \times 15\ \mu m^2$) through which particles suspended in liquid can be moved by applying vacuum pressure at the outlet reservoir of the channel. These particles are optically excited by a perpendicularly intersecting waveguide whose core consists of high refractive index PDMS.[41] Fluorescent or scattered light from the target particle is collected through the fluidic channel into a collection waveguide that then widens into an MMI section as shown. All waveguide types are located in the same layer and created in the same lithography step, ensuring that the addition of the spectrometer does not add any fabrication steps. For imaging of the scatter patterns, we rely on natural defects in the PDMS without adding surface roughness. As individual gold microbeads flow through the channel, they are excited with red laser light, blue laser light, and a combination of both while the MMI section is imaged from the top to analyze the Rayleigh scattered light signals. Camera frames from blue, red, and red & blue signals are shown in Fig. 5(c), and they exhibit clear differences. A detailed description of the camera frame analysis and their independent confirmation as scatter events is provided in the supplementary material. We recorded a total of 45 MMI images, each corresponding to a single-particle Raleigh scattering event. Distinguishing the scattering events represents a classification task with three distinct categories (red, blue, and red & blue), which is fundamentally different from the regression

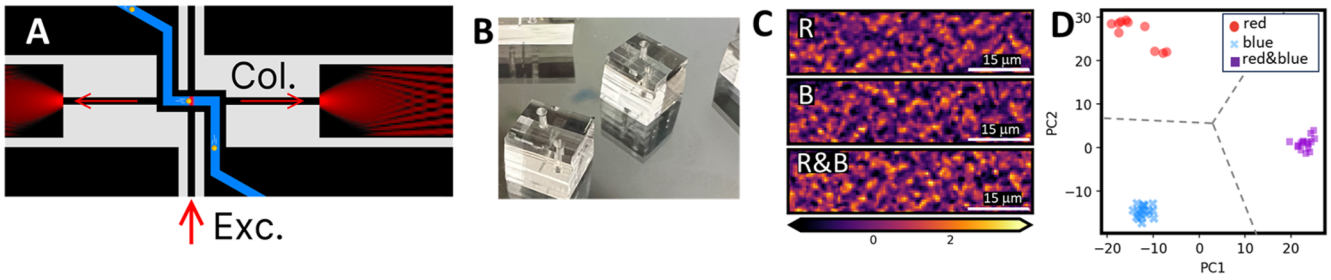

FIG. 5. Particle classification with lab-on-chip MMI spectrometer. (a) Schematic view of PDMS optofluidic chip with integrated MMI spectrometer. Light coupled into solid-core waveguide excites metallic microbeads moving through a microfluidic channel (blue). The Rayleigh scattered signal from a bead is guided into an MMI section by a collection waveguide for spectral analysis. (b) Photograph of lab-on-chip devices. (c) Average MMI scatter patterns for bead scattering of red (R), blue (b), and red & blue (R & B) light, respectively. (d) Principal component analysis of scatter images reveals clearly separated clusters for error-free detection of all three spectral signals.

algorithm used above to determine a continuous spectrum. Consequently, a different machine learning algorithm that is better suited for this task can be chosen. We use principal component analysis (PCA)—an unsupervised learning algorithm that transforms the information contained in the pixel intensities of a 28 × 120 pixels image (equivalent to a 3360-dimensional feature space) into a reduced two-dimensional space.[44] First, a 45 × 3360 feature matrix is formed by flattening and stacking the standardized (zero mean and unit variance) MMI images. From this, the 3360 × 3360 elements covariance matrix is then calculated, which, upon eigenvalue decomposition, gives the orthogonal principal components of the data. The two 3360 × 1 eigenvectors corresponding to the two largest eigenvalues are selected and multiplied with the feature matrix. Each row in the resulting 45 × 2 matrix represents the two principal components (PC1, PC2) with the highest variances for each MMI image and are displayed in Fig. 5(d). Three strongly distinct groups are observed and each single-particle scatter signal is correctly classified in the corresponding group. This demonstrates that different machine learning methods can be used to analyze the MMI scatter images to handle the most common spectroscopy tasks. The waveguide-based spectrometer is fully compatible with established optofluidic device architectures, and the ability to implement both classification and continuous spectral analysis will enable numerous analytical functions such as multiplexed fluorescence detection and Raman spectroscopy.

IV. DISCUSSION AND CONCLUSION

We have introduced a new waveguide-based miniaturized spectrometer that combines high performance with planar photonic integration. By imaging wavelength-dependent light propagation patterns in multi-mode interference waveguides and analyzing them with different machine learning techniques, both continuous and discrete spectra can be analyzed on-chip with the performance of commercial dispersive spectrometers. The reported performance of the device was achieved without maximizing the stability of the experiment, e.g., via active temperature control of the chip. External factors such as mechanical and temperature stability can be addressed to further improve the device performance. The intrinsic advantages of this planar photonic approach were demonstrated with a 1 × 4 spectrometer array and the incorporation of a spectral analysis section in an optofluidic lab-on-chip device for single particle analysis. This architecture offers numerous future integration possibilities, including placing the MMI waveguide directly with an image sensor, e.g., in a cellphone or on the same chip, and the creation of a standardized input interface by direct attachment of optical fibers with the chip. Doing so will create spectrometers for a broad array of use cases, especially for portable and remote operations in the field.

SUPPLEMENTARY MATERIAL

See the supplementary material for additional details on the waveguide fabrication process, design details, and training process of the convolutional neural network; optical setups for spectrometer characterization; performance evaluation in the visible wavelengths; sunlight spectral analysis; and biosensing application principle and experiments.

ACKNOWLEDGMENTS

This work was supported by the National Science Foundation (Grant Nos. 2206259 and 2206564). We thank M. J. N. Sampad for assistance with the laser instrumentation, D. Mendez for assistance with the solar spectrum measurements, and T. D. Yuzvinsky for assistance with SEM imaging in the W. M. Keck Center for Nanoscale Optofluidics Facilities at UC Santa Cruz.

AUTHOR DECLARATIONS

Conflict of Interest

The authors have no conflicts to disclose.

Author Contributions

M.N.A. and V.G. contributed equally to this work.

Md Nafiz Amin: Investigation (equal); Methodology (equal); Writing – original draft (equal). **Vahid Ganjalizadeh**: Investigation (equal); Methodology (equal); Writing – original draft (equal). **Tyler J. Adams**: Investigation (supporting); Writing – review & editing

(equal). **Porter B. Dixon**: Investigation (supporting); Writing – review & editing (equal). **Zoe Weber**: Investigation (supporting); Writing – review & editing (equal). **Matthew DeMartino**: Investigation (supporting); Writing – review & editing (equal). **Kevin Bundy**: Conceptualization (lead); Funding acquisition (lead); Supervision (lead); Writing – review & editing (equal). **Aaron R. Hawkins**: Conceptualization (lead); Funding acquisition (lead); Supervision (lead); Writing – original draft (equal). **Holger Schmidt**: Conceptualization (lead); Funding acquisition (lead); Methodology (equal); Supervision (lead); Writing – original draft (lead).

DATA AVAILABILITY

The data that support the findings of this study are available from the corresponding author upon reasonable request.

REFERENCES

[1]M. Mayor and D. Queloz, "A Jupiter-mass companion to a solar-type star," Nature **378**(6555), 355–359 (1995).
[2]M. S. Marley and T. D. Robinson, "On the cool side: Modeling the atmospheres of Brown dwarfs and giant planets," Annu. Rev. Astron. Astrophys. **53**, 279–323 (2015).
[3]A. Downes and A. Elfick, "Raman spectroscopy and related techniques in biomedicine," Sensors **10**(3), 1871–1889 (2010).
[4]J. Seo, Y. Sim, J. Kim *et al.*, "PICASSO allows ultra-multiplexed fluorescence imaging of spatially overlapping proteins without reference spectra measurements," Nat. Commun. **13**(1), 2475 (2022).
[5]G. K. Geiss, R. E. Bumgarner, B. Birditt *et al.*, "Direct multiplexed measurement of gene expression with color-coded probe pairs," Nat. Biotechnol. **26**(3), 317–325 (2008).
[6]Y. Xiong, Q. Huang, T. D. Canady *et al.*, "Photonic crystal enhanced fluorescence emission and blinking suppression for single quantum dot digital resolution biosensing," Nat. Commun. **13**(1), 4647 (2022).
[7]A. Stambaugh, J. W. Parks, M. A. Stott *et al.*, "Optofluidic multiplex detection of single SARS-CoV-2 and influenza A antigens using a novel bright fluorescent probe assay," Proc. Natl. Acad. Sci. U. S. A. **118**(20), e2103480118 (2021).
[8]Z. Yang, T. Albrow-Owen, W. Cai, and T. Hasan, "Miniaturization of optical spectrometers," Science **371**, 6528 (2021).
[9]R. F. Wolffenbuttel, "State-of-the-art in integrated optical microspectrometers," IEEE Trans. Instrum. Meas. **53**(1), 197–202 (2004).
[10]T. A. Kwa and R. F. Wolffenbuttel, "Integrated grating/detector array fabricated in silicon using micromachining techniques," Sens. Actuators, A **31**, 259–266 (1992).
[11]K. D. Long, E. V. Woodburn, H. M. Le *et al.*, "Multimode smartphone biosensing: The transmission, reflection, and intensity spectral (TRI)-analyzer," Lab Chip **17**(19), 3246–3257 (2017).
[12]M. A. Aguirre, K. D. Long, and B. T. Cunningham, "Spectrometric smartphone-based system for ibuprofen quantification in commercial dosage tablets," J. Pharm. Sci. **108**(8), 2593–2598 (2019).
[13]E. V. Woodburn, K. D. Long, and B. T. Cunningham, "Analysis of paper-based colorimetric assays with a smartphone spectrometer," IEEE Sensors J. **19**(2), 508–514 (2019).
[14]P. J. Lapray, X. Wang, J. B. Thomas, and P. Gouton, "Multispectral filter arrays: Recent advances and practical implementation," Sensors **14**(11), 21626–21659 (2014).
[15]S. W. Wang, C. Xia, X. Chen *et al.*, "Concept of a high-resolution miniature spectrometer using an integrated filter array," Opt. Lett. **32**(6), 632–634 (2007).
[16]A. V. Velasco, P. Cheben, P. J. Bock *et al.*, "High-resolution Fourier-transform spectrometer chip with microphotonic silicon spiral waveguides," Opt. Lett. **38**(5), 706–708 (2013).
[17]A. Li and Y. Fainman, "On-chip spectrometers using stratified waveguide filters," Nat. Commun. **12**(1), 2704 (2021).
[18]H. H. Yoon, H. A. Fernandez, F. Nigmatulin *et al.*, "Miniaturized spectrometers with a tunable van der Waals junction," Science **378**, 296–299 (2022).
[19]B. Redding, S. F. Liew, R. Sarma, and H. Cao, "Compact spectrometer based on a disordered photonic chip," Nat. Photonics **7**(9), 746–751 (2013).
[20]C. Brown, A. Goncharov, Z. S. Ballard *et al.*, "Neural network-based on-chip spectroscopy using a scalable plasmonic encoder," ACS Nano **15**(4), 6305–6315 (2021).
[21]B. Redding, S. Fatt Liew, Y. Bromberg *et al.*, "Evanescently coupled multimode spiral spectrometer," Optica **3**(9), 956–962 (2016).
[22]C. Yao, K. Xu, W. Zhang *et al.*, "Integrated reconstructive spectrometer with programmable photonic circuits," Nat. Commun. **14**(1), 6376 (2023).
[23]N. H. Wan, F. Meng, T. Schroder *et al.*, "High-resolution optical spectroscopy using multimode interference in a compact tapered fibre," Nat. Commun. **6**(1), 7762 (2015).
[24]B. Redding and H. Cao, "Using a multimode fiber as a high-resolution, low-loss spectrometer," Opt. Lett. **37**(16), 3384–3386 (2012).
[25]Q. Cen, S. Pian, X. Liu *et al.*, "Microtaper leaky-mode spectrometer with picometer resolution," eLight **3**(1), 9 (2023).
[26]L. B. Soldano and E. C. M. Pennings, "Optical multi-mode interference devices based on self-imaging: Principles and applications," J. Lightwave Technol. **13**(4), 615–627 (1995).
[27]D. Ozcelik, J. W. Parks, T. A. Wall *et al.*, "Optofluidic wavelength division multiplexing for single-virus detection," Proc. Natl. Acad. Sci. U. S. A. **112**(42), 12933–12937 (2015).
[28]A. Geron, *Hands-On Machine Learning with Scikit-Learn, Keras, & TensorFlow*, 3rd ed. (O'Reilly, 2022), pp. 372–376.
[29]E. Hubble, "A relation between distance and radial velocity among extra-galactic nebulae," Proc. Natl. Acad. Sci. U. S. A. **15**(3), 168–173 (1929).
[30][K. Bundy, K. B. Westfall, N. MacDonald *et al.*, "The Keck-FOBOS spectroscopic facility: Conceptual design," SPIE Proc. **11447**, 278–291 (2020).
[31]D. J. Schlegel, J. A. Kollmeier, G. Aldering *et al.*, "The MegaMapper: A stage-5 spectroscopic instrument concept for the study of inflation and dark energy," arXiv:2209.04322 (2022).
[32]N. Jovanovic, P. Gatkine, N. Anugu *et al.*, "2023 astrophotonics roadmap: Pathways to realizing multi-functional integrated astrophotonic instruments," J. Phys. Photonics **5**(4), 042501 (2023).
[33]R. S. DeJong, O. Agertz, A. A. Berbel *et al.*, "4MOST: Project overview and information for the first call for proposals," arXiv:1903.02464 (2019).
[34]J. D. Simon, S. Birrer, K. Bechtol *et al.*, "Testing the nature of dark matter with extremely large telescopes," Bull. AAS **51**(3), (2019), see https://baas.aas.org/pub/2020n3i153.
[35]A. Aghamousa, J. Aguilar, J. Ahlen *et al.*, "The DESI experiment Part I: Science, targeting, and survey design," arXiv:1611.00036v2 (2016).
[36]A. J. Bechter, J. Crass, J. Tesch *et al.*, "Characterization of single-mode fiber coupling at the large binocular telescope," Publ. Astron. Soc. Pac. **132**(1007), 015001 (2020).
[37]M. A. Butt, G. S. Voronkov, E. P. Grakhova *et al.*, "Environmental monitoring: A comprehensive review on optical waveguide and fiber-based sensors," Biosensors **12**(11), 1038 (2022).
[38]X. Fan and I. M. White, "Optofluidic microsystems for chemical and biological analysis," Nat. Photonics **5**(10), 591–597 (2011).
[39]H. Schmidt and A. R. Hawkins, "The photonic integration of non-solid media using optofluidics," Nat. Photonics **5**(10), 598–604 (2011).
[40]P. Minzioni, R. Osellame, C. Sada *et al.*, "Roadmap for optofluidics," J. Opt. **19**(9), 093003 (2017).
[41]J. W. Parks and H. Schmidt, "Flexible optofluidic waveguide platform with multi-dimensional reconfigurability," Sci. Rep. **6**(1), 33008 (2016).
[42]G. G. Meena, A. Jain, J. W. Parks *et al.*, "Integration of sample preparation and analysis into an optofluidic chip for multi-target disease detection," Lab Chip **18**(23), 3678–3686 (2018).
[43]T. Sano, H. Zhang, R. Losakul, and H. Schmidt, "All-in-one optofluidic chip for molecular biosensing assays," Biosensors **12**(7), 501 (2022).
[44]A. Geron, *Hands-On Machine Learning with Scikit-Learn, Keras, and TensorFlow*, 3rd ed. (O'Reilly, 2022), pp. 243–252.